Geophys. J. Int. (1995) **122,** 1045–1061

Causes of low-frequency ground motion amplification in the Salt Lake Basin: the case of the vertically incident *P* wave

Kim B. Olsen* and Gerard T. Schuster
Department of Geology and Geophysics, University of Utah, Salt Lake City, UT 84112, *USA*

Accepted 1995 April 6. Received 1995 March 30; in original form 1994 October 8

SUMMARY

We use simulations of 1-D, 2-D and 3-D wave propagation to identify the major causes of low-frequency (0.2–1.2 Hz) seismic amplification in the Salt Lake Basin. For a simple two-layer basin model and a vertically incident *P* wave, we examine how amplification is influenced by mode conversion, surface-wave generation, impedance effects at the sediment–bedrock boundary, resonance, and 2-D and 3-D focusing and scattering. Results show the following.

(1) Approximately 30 per cent of the total cumulative kinetic energy at the Salt Lake Valley floor consists of shear-wave energy generated by *P*-to-*S* converted waves and surface waves. The surface waves appear to be generated primarily along the edges of the basin, and the instantaneous S/P energy ratio in the sedimentary layer is as large as 3.

(2) The largest peak particle velocity at the free surface is due to the direct *P* wave. The value is roughly predicted by the transmission coefficient of 1.46 at the sediment–bedrock interface, i.e. a normally incident *P* wave in the stiff bedrock will be magnified in amplitude by 1.46 times as it enters the softer sediments.

(3) The low-frequency elastic response of the two-layer Salt Lake Basin model is characterized by surface-wave propagation and resonance from vertically interfering waves.

(4) The peak particle velocities, cumulative kinetic energies, and mean spectral magnitudes computed from the 2-D (1-D) synthetics underestimate the values computed from the 3-D synthetics by up to 40 per cent (48 per cent) along a profile above the deepest part of the basin model. The 2-D and 1-D signal duration times underestimate the 3-D values by up to 59 and 94 per cent, respectively. Our results suggest that 2-D basin modelling may yield good approximations to the 3-D ground motion amplification above the deepest part of the Salt Lake Basin.

Our results show that several mechanisms contribute significantly to low-frequency seismic amplification in the semi-consolidated sediments of the Salt Lake Basin—*P*-to-*S* wave conversion, surface-wave generation, impedance effects at the sediment–bedrock boundary, and resonance. Future attempts to estimate ground motion amplification in the Salt Lake Basin should therefore account for the amplification effects of all these mechanisms.

Key words: finite-difference methods, *P* waves, sedimentary basins, seismic modelling, wave propagation.

INTRODUCTION

It is well known that seismic waves are amplified in alluvial basins, relative to the surrounding bedrock (e.g. Bard & Bouchon 1980a,b; Kawase & Aki 1989). Recent examples include the devastation in Mexico City caused by the 1985 M_S 8.1 Michoacan, Mexico, earthquake (Anderson *et al.* 1986), and the damage caused by the 1989 Loma Prieta, California, earthquake in the cities of San Francisco and Oakland (US Geological Survey Staff 1990). It is therefore imperative to understand the causes of ground motion

* Now at: Institute for Crustal Studies, University of California at Santa Barbara, Santa Barbara, CA 93106-1100, USA.

amplification in alluvial basins, in order to mitigate the loss of life and property during major earthquakes. Note that, in this paper, we use the term 'alluvial basin' in a generalized sense to refer to structural basins filled with sediments of various origins, not just fluvial.

Previous studies have shown that amplification of seismic waves in alluvial basins is controlled by several distinct processes.

(1) *P*-to-*S* wave conversion and surface-wave generation. Evidence for significant *P*-to-*S* wave conversion at the base of sedimentary layers has been reported in several studies, for example by Hough (1990) in the San Francisco Bay area. The generation of surface waves from body waves incident at the edges of basins was pointed out by Bard & Bouchon (1980a, b), Bard *et al.* (1988), Horike (1988), Vidale & Helmberger (1988), Kawase & Aki (1989), Horike, Uebayashi & Takeuchi (1990), Frankel *et al.* (1991), Frankel & Vidale (1992), Frankel (1993) and Yomogida & Etgen (1993). These surface waves are often characterized by somewhat large amplitudes that significantly influence the site amplification.

(2) Impedance effects. Conservation of energy demands that the amplitude of a signal increases as it travels from a stiff rock to a softer rock. Joyner, Warrick & Fumal (1981), Williams, King & Tinsley (1993) and others used formulae based on the impedance contrast at the sediment–bedrock boundary partially to explain site amplification in alluvial basins.

(3) Resonance effects. For a layered medium, seismic resonance is the constructive reinforcement of multiply reflected waves where the layer thickness is tuned to the seismic wavelength. Bard & Bouchon (1985) and Rial, Saltzman & Ling (1992) showed the importance of deep-basin resonance for site amplification in alluvial basins, while Hill & Levander (1984), Kawase & Aki (1989) and Olsen, Pechmann & Schuster (1995a,b) showed that reverberations in near-surface low-velocity layers significantly increase the duration of shaking.

(4) 3-D scattering. Until a few years ago, computer limitations restricted studies of site amplification in the Salt Lake Basin to 1-D and 2-D simulations (e.g. Hill *et al.* 1990; Murphy 1989; Benz & Smith 1988). However, recent work (e.g. Horike 1988; Horike *et al.* 1990; Frankel 1993) showed that there can be major differences in the seismic responses of 2-D and 3-D basin models. These differences include larger amplitudes and a longer duration of shaking obtained from 3-D basin models compared to those obtained from 2-D models.

(5) Topographic scattering. The site amplification in the Salt Lake Valley due to scattering from the Wasatch Mountains was examined by Xu (1995, in preparation) and Olsen *et al.* (1994a) using 2-D simulations. Xu found that, for a vertically incident plane *SH*-wave source, the signal duration and cumulative kinetic energy in the Salt Lake Valley were increased by more than 15 per cent when seismic scattering from the Wasatch Mountains was taken into account. The scattered energy was maximal along the peaks of the Wasatch Mountains. However, the change in spectral ratios of ground motions between rock and sediment sites caused by scattering from the topography was found to be negligible. For a vertically incident plane *P*-wave source, Olsen *et al.* (1995a) found that seismic scattering from the neighbouring mountains increased the cumulative kinetic energy by about 40 per cent.

(6) Anelastic attenuation. Frankel & Vidale (1992), Frankel (1993), and Olsen *et al.* (1995a,b) showed that attenuation is a major limiting factor to the duration of shaking in alluvial valleys.

Olsen *et al.* (1995a,b) found that 3-D simulations in a simple two-layer Salt Lake Basin model were able roughly to predict the recorded peak particle velocities for a teleseism and for an open-mine blast. The fair agreement between the observed and simulated amplification patterns prompts the following question: what are the salient causes of low-frequency site amplification in the Salt Lake Valley in this simple model? In this paper, we answer this question by analysing mechanisms (1) to (4) described above for a plane *P* wave vertically incident onto several models of the Salt Lake Basin. Specifically, we use 2-D wavefield separation and a 3-D acoustic simulation to quantify the degrees of *P*-to-*S* wave conversion and surface-wave generation in the basin model. We then estimate the amplification due to impedance effects at the sediment–bedrock interface and to resonance from vertical interference of multiply reflected waves. Finally, we examine the validity of using 1-D and 2-D simulations for estimating the seismic response of the 3-D Salt Lake Basin model. This issue is important because the presence of significant 3-D effects may (a) alter conclusions based on 1-D and 2-D basin amplification studies in the Salt Lake Basin, and (b) dictate the use of computationally intensive 3-D modelling in future Salt Lake Basin amplification studies.

SIMULATION OF 3-D WAVE PROPAGATION

Salt Lake Basin model

We select the 3-D model of the Salt Lake Basin used by Olsen *et al.* (1995a,b; Fig. 1) for our analysis. This simple two-layer model consists of sediments surrounded by bedrock. The boundary between sediments and bedrock was estimated by 3-D inversion of gravity data constrained by three seismic reflection lines and 40 water-well logs (Radkins 1990). The most reliable part of the basin model is the northern part, because of its proximity to the seismic reflection lines. The estimate of the basin model is less reliable in the south-western part, where recent seismic refraction studies suggest that the thickness of the sediments is underestimated by up to 0.4 km in some places (C. Zhou, 1993, personal communication).

Hill *et al.* (1990) and Murphy (1989) included three layer boundaries in their 2-D Salt Lake Basin models: R1, separating unconsolidated and semi-consolidated sediments; R2, separating semi-consolidated and consolidated sediments; and R3, separating consolidated sediments and bedrock. Their 2-D simulations indicated that the dominant contributions to low-frequency amplification in the Salt Lake Valley are reflections and surface waves associated with the R1 and R2 boundaries. Since the R2 boundary is

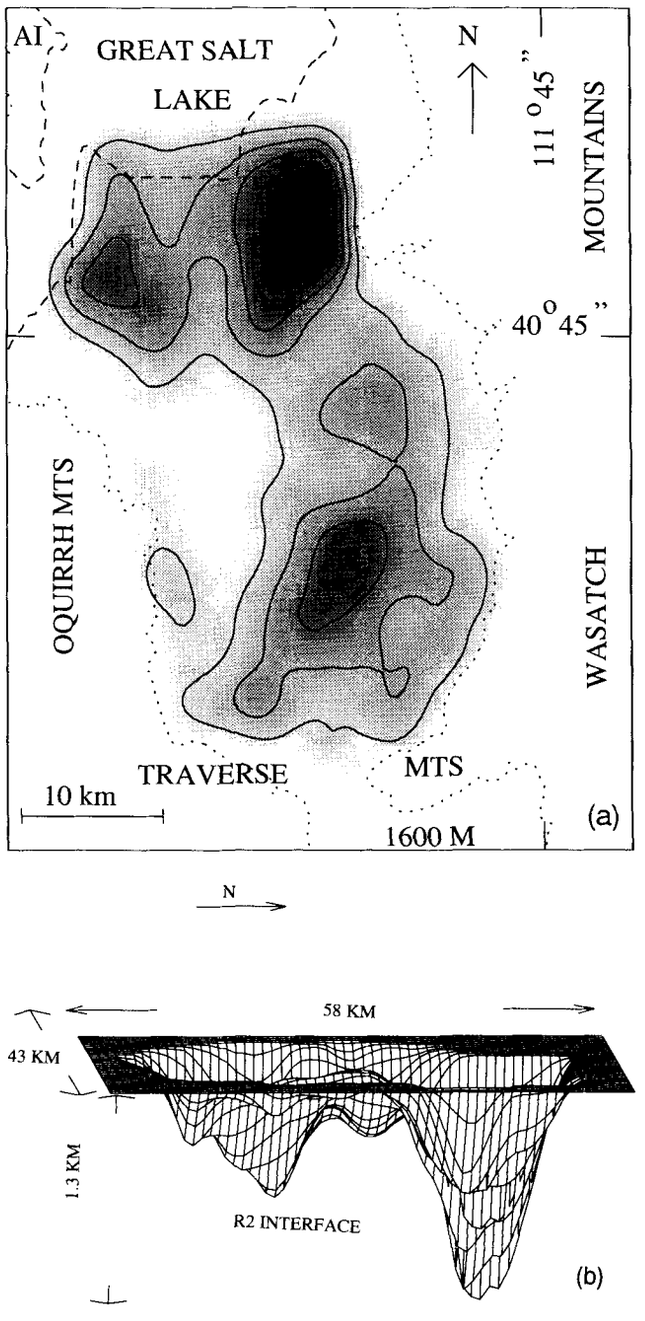

Figure 1. Salt Lake Basin model. (a) Map of the Salt Lake Basin. The contours (200 m interval, shallowest contour at a depth of 150 m below the valley floor) and the shading depict the depth of the R2 interface (the sediment–bedrock boundary) below the valley floor; darker shading indicates greater depth to R2. The three deepest parts of the basin model will be referred to according to location as the NE bowl, the NW bowl and the southern bowl of the basin. The dotted and dashed lines depict an elevation of 1600 m above sea-level and the shoreline of the Great Salt Lake, respectively. AI is Antelope Island. (b) 3-D perspective of the R2 interface. The 3-D modelling parameters are listed in Table 1.

associated with the biggest impedance contrast in the 2-D models, Olsen *et al.* (1995a,b) used this interface as the sediment–bedrock interface in their 3-D Salt Lake Basin model.

The density and the *P*-wave velocity of the bedrock are taken from Hill *et al.* (1990), who obtained them from well logs. The *P*-wave velocity of the sediments was taken to be 2.2 km s^{-1}, 10 per cent lower than that given by Hill *et al.* (1990) for the semi-consolidated sediments. The lower velocity for the semi-consolidated sediments was a compromise between excluding the unconsolidated sediments and keeping the sediment velocity within limits dictated by the computational power. *S*-wave velocities are approximated by dividing the *P*-wave velocities by $\sqrt{3}$. Nicholson & Simpson (1985) found this approximation to be reasonable for bedrock deeper than ≈2–3 km by analysing *P* and *S* arrival times from microearthquakes; however, they also found that V_p/V_s ratios in rock typically increase to values of around 2.0 at shallower depths.

Finite-difference scheme

We use a staggered-grid finite-difference scheme to solve the 3-D elastic equations of motion (Levander 1988), where the accuracy is fourth-order in space and second-order in time. The numerical implementation of the 3-D scheme is described in Olsen (1994, Chapter 1, Appendix A). The simulations were carried out on an IBM 3090 supercomputer using approximately 320 Mbytes of physical memory.

The basin model is discretized with a grid-point spacing of 0.15 km; this corresponds to approximately 7 grid-points per minimum shear wavelength of 1.1 km, which limits the numerical dispersion error to less than 12 per cent (see Olsen 1994, Chapter 1, Appendix B). The Salt Lake Basin model (approximately 58 km × 43 km × 9 km) is discretized into 384 × 288 × 60 (=6.6 million) grid-points. The sides of the computational model are padded with homogeneous regions of attenuative material to limit reflections from the grid boundaries (Cerjan *et al.* 1985). The 3-D modelling parameters are listed in Table 1.

For the 3-D simulations, we use a Ricker wavelet source function with a bandwidth of approximately 0.2–1.2 Hz (Fig. 2). In all of the simulations discussed in this paper, the source is a plane *P* wave vertically incident onto the Salt Lake Basin model.

Table 1. 3-D modelling parameters.

Spatial discretization (km)	0.15
Temporal discretization (sec)	.013
P-wave velocity in sediments (km/sec)	2.20
S-wave velocity in sediments (km/sec)	1.27
Density in sediments (g/cm^3)	2.2
P-wave velocity in bedrock (km/sec)	5.00
S-wave velocity in bedrock (km/sec)	2.89
Density in bedrock (g/cm^3)	2.6
Number of grid points along E-W	288
Number of grid points along N-S	384
Number of grid points along vertical	60
Minimum source frequency (Hz)	0.2
Maximum source frequency (Hz)	1.2
Peak source frequency (Hz)	0.6
Number of timesteps	4616
Simulation time (sec)	60

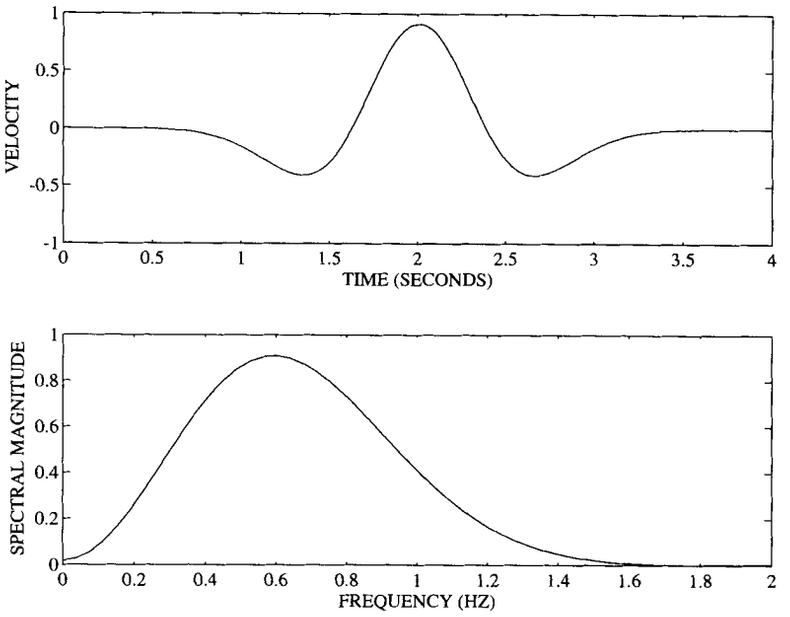

Figure 2. Velocity–time function (top) and velocity spectrum (bottom) of the Ricker wavelet source function used in the 3-D simulations.

3-D TWO-LAYER SALT LAKE BASIN MODEL RESPONSE

In this section, we analyse synthetic seismograms and ground motion parameter ratios along a profile above the deepest part of the basin model in Fig. 1.

In the following, we use the ground motion parameters defined by Olsen *et al.* (1995a).

(1) The peak particle velocity of the kth-component trace measured at location (x, y) is defined as

$$P_k(x, y) = \text{MAX}\,[|\dot{u}_k(x, y, t)|], \tag{1}$$

where $\dot{u}_k\ (x, y, t)$ is the velocity time history for the kth component, and 'MAX' indicates the maximum value of $|\dot{u}_k(x, y, t)|$ for all time t.

(2) The cumulative kinetic energy per unit volume of the kth-component trace is given as

$$E_k(x, y) = \tfrac{1}{2}\rho(x, y)\int \dot{u}_k^2(x, y, t)\, dt, \tag{2}$$

where $\rho(x, y)$ is the density, and the limits of integration are over the time interval of the simulation.

(3) The signal duration is the time interval from the P-wave arrival to the beginning of the first interval when the absolute value of the velocity stays below a threshold value for 2.6 consecutive seconds.

(4) The spectral magnitude of the kth component is defined as

$$S_k(x, y, \omega) = |\dot{U}_k(x, y, \omega)|, \tag{3}$$

where $\dot{U}_k(x, y, \omega)$ is the temporal Fourier transform of $\dot{u}_k(x, y, t)$. The last 5 s of the seismic traces are tapered by a Hanning window prior to transformation into the frequency domain. The mean spectral magnitude is found by averaging the spectrum between 0.2 and 1.2 Hz.

The above ground motion parameters are normalized to those measured at a rock site on the vertical component.

Figure 3 shows synthetic velocity seismograms along profile AB across the 3-D Salt Lake Basin model for a vertically incident plane P-wave source. These record sections show large-amplitude surface waves propagating westwards from the eastern edge of the basin, similar to those that Murphy (1989) found in her 2-D simulations. Note that these surface waves are much stronger on the E–W component than on the N–S component, and propagate along the profile with a velocity roughly equal to the shear velocity of the sediments. These observations suggest that the surface waves are mainly Rayleigh waves propagating along the E–W axis. Fig. 4 plots the ground motion parameter ratios along profile AB from which we observe the following.

(1) The largest peak particle velocity ratio is that of the direct wave on the vertical-component records (see Fig. 3). Section 2.6 shows that this peak particle velocity ratio of about 1.5 is predicted by the transmission coefficient at the sediment–bedrock interface.

(2) The signal duration ratios on the horizontal components are generally 1–2 times longer than those on the vertical component. This fact suggests that a significant amount of the incident energy is transformed from vertical-component to horizontal-component wave motion. We will later examine the roles of focusing, scattering and mode conversion in this transformation.

(3) The ratios of mean spectral magnitudes and cumulative kinetic energies are largest on the vertical-component records, and are generally larger in the eastern part of the basin than in the western part. These observations are consistent with the fundamental P-wave vertical resonance frequencies f_0^p of the basin. For a source

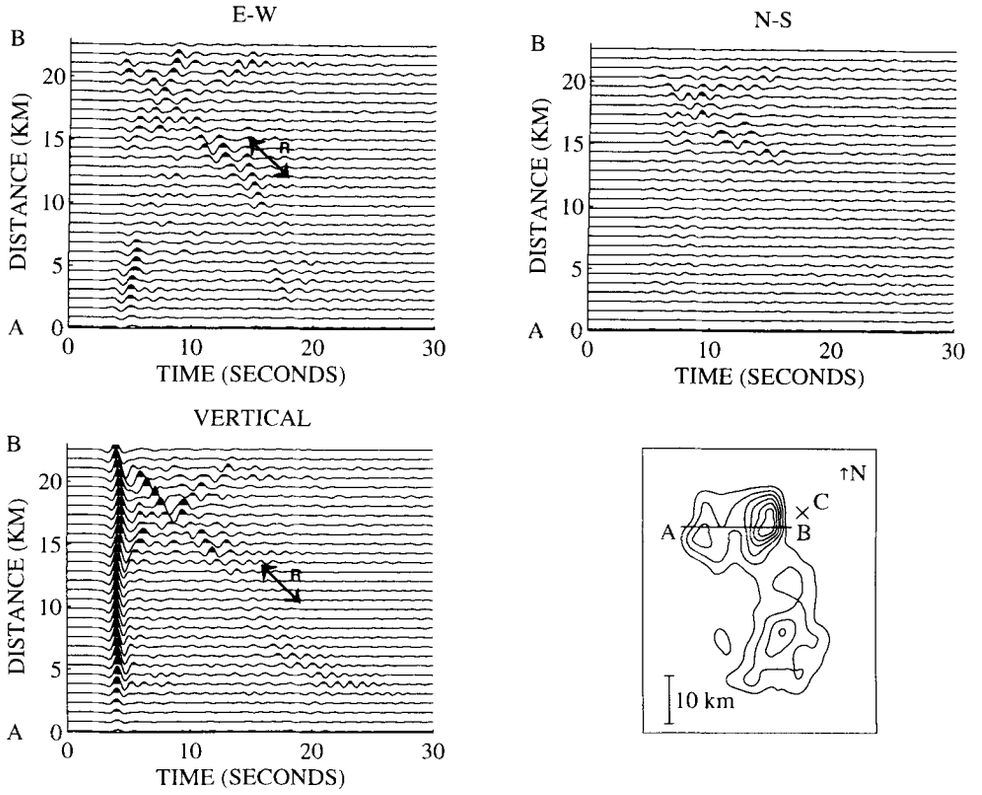

Figure 3. E–W-, N–S- and vertical-component velocity seismograms for a simulation with a vertically incident plane *P* wave in the two-layer 3-D basin model. The seismograms are for sites along profile AB shown on the map. 'R' denotes a westward propagating Rayleigh wave. The seismic amplitudes are directly comparable to those shown in Figs 9, 12 and 13. The contour map shows the depth to the R2 interface at a contour interval of 200 m. The shallowest contour is at a depth of 150 m below the valley floor. 'x' indicates the location of the reference rock site C.

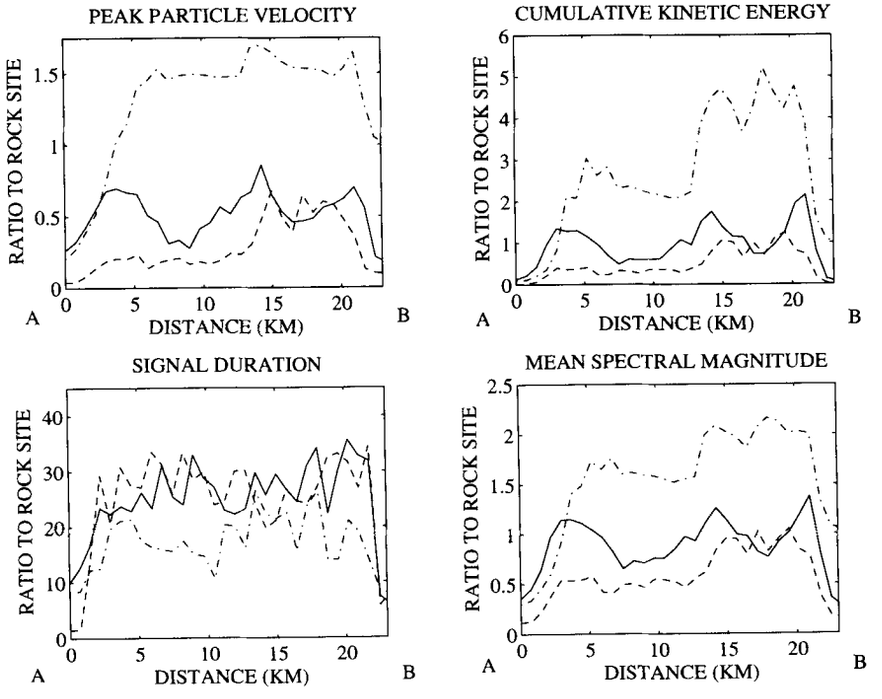

Figure 4. Ratios of peak particle velocities, cumulative kinetic energies, signal duration times and mean spectral magnitudes for the E–W (solid), N–S (dashed) and vertical (dot–dashed) components along profile AB (see Fig. 3). The values are normalized to those on the vertical component at the rock site C (Fig. 3).

with a 0.2–1.2 Hz bandwidth, *P*-wave resonance is promoted in the eastern part of the basin, ($f_0^p \approx 0.6$ Hz), while it is hindered in the western part ($f_0^p \approx 1.3$ Hz).

The two-layer Salt Lake Basin response for a vertically incident *P* wave suggests that strong Rayleigh waves are generated at the basin edges. In the following section, we use wavefield separation and an acoustic simulation to estimate the extent of *P*-to-*S* wave conversion and surface-wave generation in the two-layer Salt Lake Basin model.

P-TO-*S* WAVE CONVERSION AND SURFACE-WAVE GENERATION

Horike (1988), Horike *et al.* (1990) and Frankel (1993) showed that mode conversion can generate strong arrivals in 3-D basin models. It is therefore important to assess the significance of converted waves in ground motion amplification in the Salt Lake Basin. In this section, we analyse the effects of *P*-to-*S* wave conversion and surface-wave generation in two ways: (1) we formulate a technique to separate *P* and *S* waves, test the procedure in a 2-D half-space model, and then apply the method to a 2-D wavefield simulated in a vertical cross-section of the Salt Lake Basin model; and (2) we estimate the amount of converted body waves and surface waves by examining the difference between the 3-D two-layer elastic basin response and the equivalent acoustic basin response.

Wavefield separation technique

We start with the elastic wave equation for a homogeneous medium:

$$\rho\ddot{\mathbf{u}} = (\lambda + 2\mu)\nabla(\nabla \cdot \mathbf{u}) - \mu\nabla \times \nabla \times \mathbf{u} + \mathbf{f}, \tag{4}$$

where $\mathbf{u}$ is the displacement vector, ρ is density, λ and μ are the Lamé coefficients and $\mathbf{f}$ is an imposed body force vector (Aki & Richards 1980, p. 64). Dellinger & Etgen (1990) suggested that the total wavefield $\mathbf{u}$ can be separated into a compressional part,

$$V_p^2\nabla(\nabla \cdot \mathbf{u}), \tag{5}$$

and a shear part,

$$V_s^2\nabla \times \nabla \times \mathbf{u}. \tag{6}$$

Here $V_p = \sqrt{(\lambda + 2\mu)/\rho}$ and $V_s = \sqrt{\mu/\rho}$ are the *P*- and *S*-wave velocities, respectively. This separation is possible because the *S* and *P* waves are annihilated under the $\nabla \cdot$ and $\nabla \times$ operators, respectively.

We use a similar approach to separate the *S* and *P* waves in our simulations. The *P*- and *S*-wave particle velocities may be found from eq. (4) as follows:

$$\dot{\mathbf{u}}_P(\mathbf{x}, t) = V_P^2\int_0^t \nabla\left[\nabla \cdot \int_0^{t'} \dot{\mathbf{u}}(\mathbf{x}, t'')\, dt''\right] dt', \tag{7}$$

and

$$\dot{\mathbf{u}}_S(\mathbf{x}, t) = V_s^2\int_0^t \nabla \times \left[\nabla \times \int_0^{t'} \dot{\mathbf{u}}(\mathbf{x}, t'')\, dt''\right] dt', \tag{8}$$

where $\dot{\mathbf{u}} = \dot{\mathbf{u}}_P + \dot{\mathbf{u}}_S$ and the above integrands are given for the 2-D case by

$$\nabla(\nabla \cdot \mathbf{u}) = \left(\frac{\partial^2 u}{\partial x^2} + \frac{\partial^2 w}{\partial x\, \partial z}\right)\mathbf{i} + \left(\frac{\partial^2 u}{\partial x\, \partial z} + \frac{\partial^2 w}{\partial z^2}\right)\mathbf{k}, \tag{9}$$

$$\nabla \times \nabla \times \mathbf{u} = \left(\frac{\partial^2 w}{\partial x\, \partial z} - \frac{\partial^2 u}{\partial z^2}\right)\mathbf{i} + \left(\frac{\partial^2 u}{\partial x\, \partial z} - \frac{\partial^2 w}{\partial x^2}\right)\mathbf{k}. \tag{10}$$

Here, u and w are the horizontal and vertical displacements, respectively, and $\mathbf{i}$ and $\mathbf{k}$ are horizontal and vertical unit vectors, respectively.

We compute the instantaneous *P* and *S* kinetic energies as, respectively,

$$E_P = \tfrac{1}{2}\rho\, |\dot{\mathbf{u}}_P|^2, \tag{11}$$

and

$$E_S = \tfrac{1}{2}\rho\, |\dot{\mathbf{u}}_S|^2. \tag{12}$$

Note that the separation procedure is only applicable for homogeneous media; this means that the method is not applicable at the sedimentary interfaces and at the free surface in our two-layer Salt Lake Basin model.

Test of the separation technique in a half-space model

The separation procedure is now tested in a half-space model using a line-source. The full wavefield response is computed by a finite-difference solution to the 2-D elastic wave equation, and eqs (7) and (8) are used to separate the *P* waves from the *S* waves. The snapshots in Fig. 5 show the successful result of separating the *P* waves (left) and *S* waves (right). A comparison with the analytical solution (not shown) shows close agreement with the separated wavefields.

Separation of *P* and *S* waves in a 2-D Salt Lake Basin model

We use eqs (7) and (8) to separate the total wavefield energy into *P* and *S* energies for a 2-D simulation of a plane *P* wave vertically incident onto vertical cross-section AB of the Salt Lake Basin model (Fig. 3, Table 2). Fig. 6 shows snapshots of the separated *P* and *S* energies for the 2-D simulation; note the significant *P*-to-*S* wave conversion at the sediment–bedrock boundary and the free surface. Also note how the strong *P*-to-*S* wave conversion and reflection of *P* energy at the dipping parts of the sediment–bedrock interface (in particular at the eastern edge of the basin) generate crisscross patterns of multiply reflected and converted waves (C) propagating towards the centre of the basin. An energetic phase (R) is seen to propagate into the basin from its eastern edge, and it is identified as a Rayleigh wave by its apparent velocity of approximately 1.15 km s^{-1} and its appearance on both the *P*- and *S*-energy panels.

Figure 7 shows *P* and *S* 'energygrams' and velocity seismograms for this simulation. The energygrams are calculated for receivers located at three grid-points below the free surface in order to apply eqs (7) and (8), but they will be referred to as having been taken 'along the free

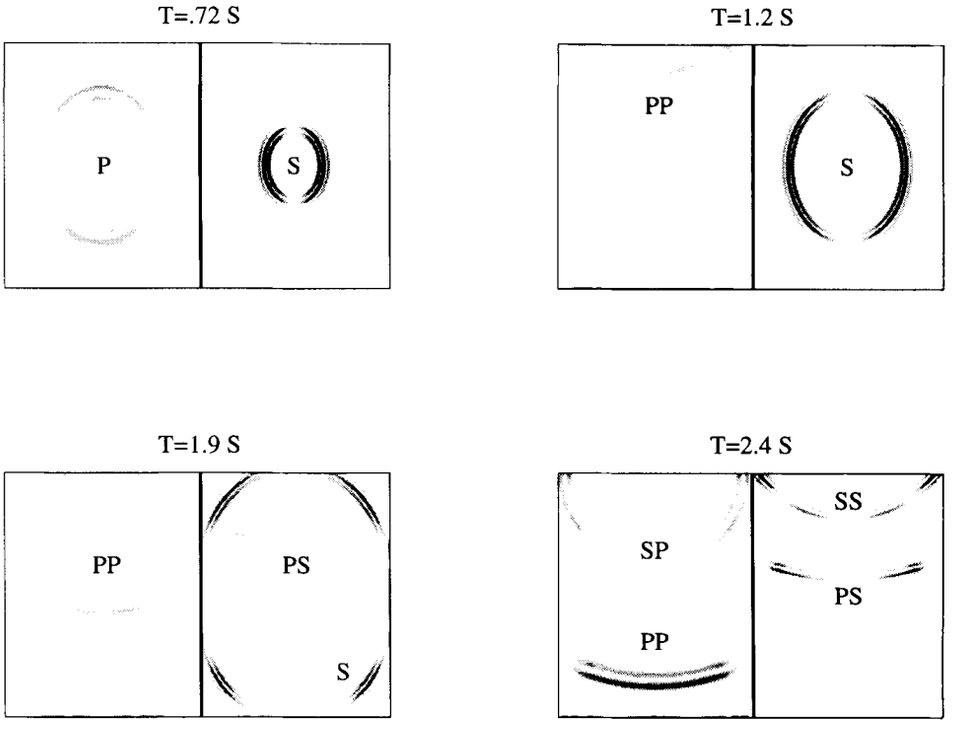

Figure 5. Snapshots of the separated wavefield originating from a vertical-force line-source in a half-space. The *P* and *S* waves are separated from the total wavefield using eqs (7) and (8), respectively. The boxes to the left (right) of the thick vertical lines show the instantaneous kinetic *P* energy (*S* energy). 'S' and 'P' denote direct *S* and *P* waves, 'SS' and 'PP' denote the reflected *S* and *P* waves at the free surface, and 'PS' and 'SP' denote, respectively, the *S* waves and *P* waves generated by mode conversion at the free surface. Vertical exaggeration is 1.25.

surface'. Note that the strong Rayleigh waves (R) identified on the snapshots in Fig. 6 are visible on both the E–W and vertical components in Fig. 7. These strong Rayleigh waves originate from the steeply dipping eastern edge of the basin boundary as in the 2-D simulations of Murphy (1989). In addition to the Rayleigh waves the seismograms also contain some arrivals identified in the snapshots as waves converted and reflected at the basin boundaries and the free surface (C). Note the similarity between the 2-D records in Fig. 7 and 3-D records in Fig. 3, except for the difference in frequency content.

To estimate the amount of *S* energy generated by mode conversion we computed the instantaneous *P* and *S* kinetic energies spatially averaged (1) throughout the basin sediments, and (2) along the free surface of the sediments. The free-surface averaging was carried out using grid-points located three nodes below the free surface. Fig. 8(a) shows the instantaneous average *S* (dashed) and *P* (solid) kinetic energies for the sediments, while Fig. 8(b) shows the ratios of average *S*-to-*P* kinetic energies for both the free surface (dashed) and the sediments (solid). After 2 s of ground motion the average *S*-to-*P* kinetic energy ratio in the sediments is larger than 1, indicating that a significant part of the body-wave energy reverberating in the sediments results from *P*-to-*S* wave conversion. The nearly 1:1 ratio of *S*-to-*P* kinetic energy just below the free surface (Fig. 8) and the comparable amounts of *P* and *S* energy in the energygrams (Fig. 7) after 4 s of ground motion are explained by the strong Rayleigh waves seen in Fig. 7.

Table 2. 2-D modelling parameters for wavefield separation.

Spatial discretization (m)	10
Temporal discretization (sec)	0.0012
Number of grid points along E-W	2901
Number of grid points along vertical	250
Minimum source frequency (Hz)	0.2
Maximum source frequency (Hz)	10
Peak source frequency (Hz)	5
Number of timesteps	20000
Simulation time (sec)	24

Elastic versus acoustic simulations

Another estimate of the amount of *P*-to-*S* wave conversion and surface-wave generation in the Salt Lake Basin model is obtained by comparing the acoustic and elastic basin responses. Any significant differences between these responses should indicate the degree to which *P* waves convert to *S* waves and surface waves.

Figure 9 shows the velocity seismograms along profile AB for an acoustic ($V_s = 0$) 3-D simulation with a *P* wave impinging vertically onto the two-layer Salt Basin model. Very little energy is seen on the horizontal-component acoustic seismograms compared to the vertical-component seismograms. This observation implies that the dominant direction of acoustic wave propagation is nearly vertical and that the acoustic energy recorded along profile AB comes mostly from in-plane scattering and focusing phenomena. The elastic signals in Fig. 3 show longer duration and significantly more energy propagating laterally along he E–W axis than do the acoustic signals in Fig. 9. This suggests that mode-converted waves contribute significantly

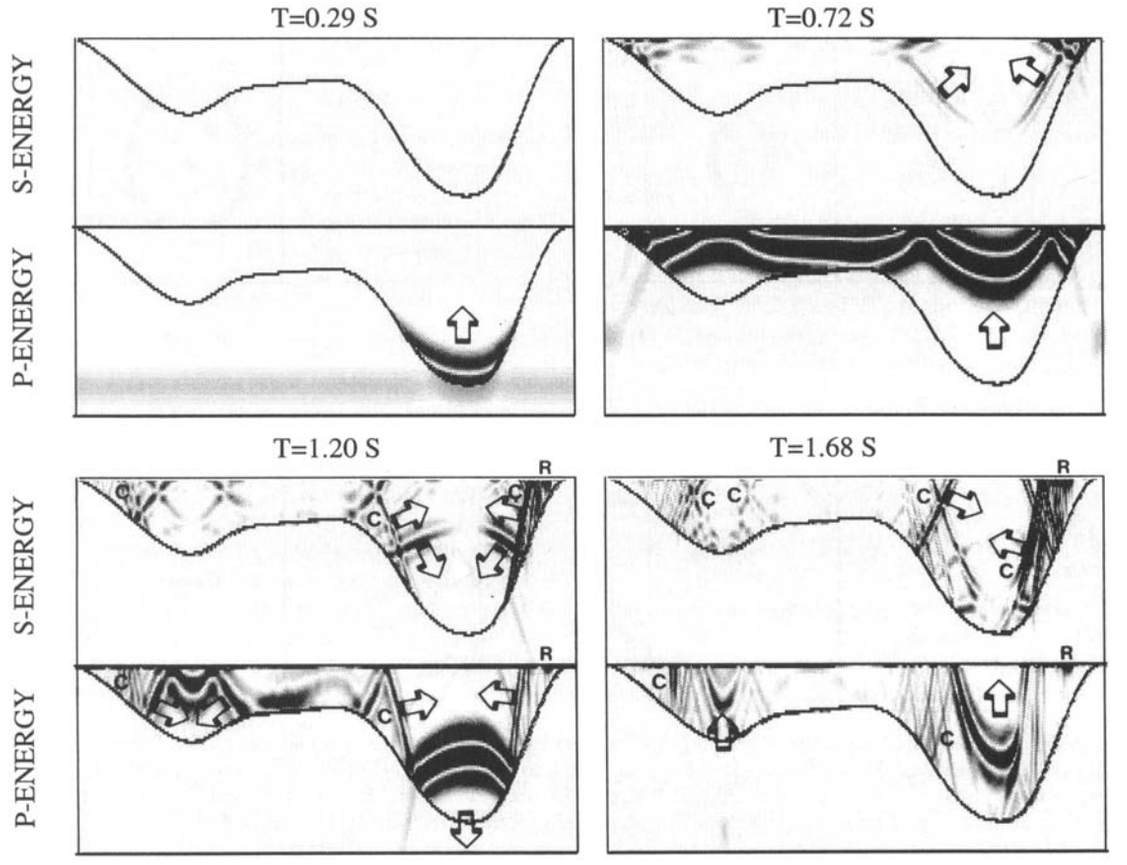

Figure 6. Snapshots of the separated wavefield for a *P* wave impinging vertically onto an E–W cross-section of the northern portion of the Salt Lake Basin model (profile AB in Fig. 3). Arrows show propagation directions, 'C' denotes the crisscross pattern of multiply reflected *P* and converted *S* waves, and 'R' denotes the Rayleigh wave. Vertical exaggeration is 3.5; the width and height of each cross-section are 24 km and 1.5 km, respectively.

to the ground motion along profile AB, which is consistent with the conclusions from the previous section. The noticeable energy on the N–S component elastic seismograms in Fig. 3 and the near-zero energy on the N–S component acoustic seismograms suggest that there are important, but not dominant, contributions to ground motion from out-of-the-plane mode-converted scattering. Table 3 quantifies these contributions by listing the maximum ground motion parameters from the acoustic simulation for the Salt Lake Valley divided by those from the elastic simulation. We find that the average cumulative elastic kinetic energy at the surface is larger than that for the acoustic simulation by approximately 30 per cent. This value roughly indicates the total amount of *S*-wave and surface-wave energy generated by mode conversion.

IMPEDANCE EFFECTS AT THE SEDIMENT–BEDROCK BOUNDARY

The transmission coefficient for a plane *P* wave vertically incident onto a flat interface between two homogeneous layers is given by

$$T = \frac{2\rho_1 V_{p1}}{\rho_1 V_{p1} + \rho_2 V_{p2}}, \tag{13}$$

where ρ and V_p are the density and *P*-wave velocity, respectively, and the subscripts 1 and 2 denote the media containing the incident and transmitted waves, respectively (e.g. Telford *et al.* 1976). This transmission coefficient formula can be used to estimate the impedance effects at the sediment–bedrock interface for the Salt Lake Basin model. Taking density and velocity values from Table 1, the sediment–bedrock transmission coefficient for the Salt Lake Basin model is calculated to be $T_{\mathrm{SED/BED}} = 1.46$. This value is comparable to the maximum vertical-component peak particle velocity ratios in the 3-D synthetics along profile AB (Fig. 4), which are those of the direct *P* arrivals. Therefore, these peak particle velocities are largely predicted by the transmission coefficient for the sediment–bedrock boundary in our two-layer Salt Lake Basin model. Apparently, focusing of the incident wave by the NE bowl of the basin model does not significantly amplify the amplitudes of the direct wave.

RESONANCE

In this section, we present mean spectral ratios in two different passbands for the ground motions computed in our 3-D simulation. We use these spectral ratios to evaluate the contribution of deep-basin resonance to site amplification in our simulations.

Figure 10 shows mean spectral ratios for the bandwidths

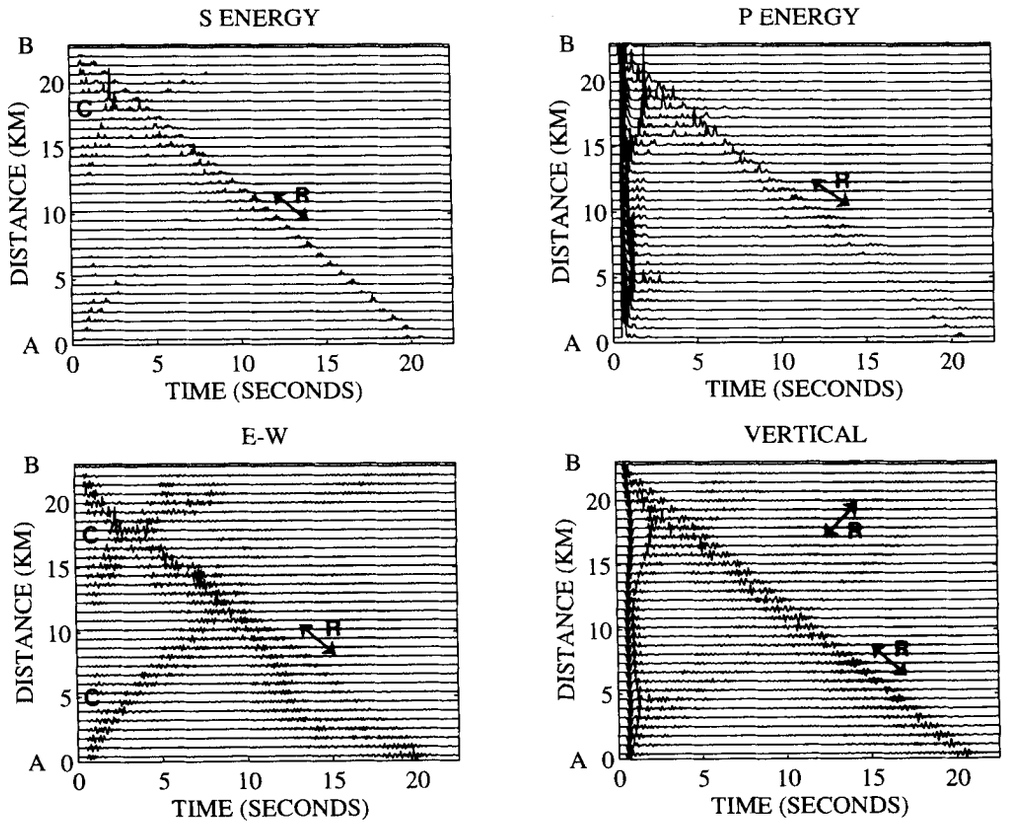

Figure 7. *S* energygrams, *P* energygrams, and E–W- and vertical-component velocity seismograms along profile AB (Fig. 3). The 2-D simulation is for a *P* wave impinging vertically onto the AB cross-section of the Salt Lake Basin model. 'C' denotes crisscross patterns of converted waves, and 'R' denotes Rayleigh waves.

0.2–0.7 and 0.7–1.2 Hz. The vertical-component mean spectral magnitudes at the bedrock site C are used as reference spectra. The 0.2–0.7 Hz mean spectral ratios for the vertical component over the deepest part (thickness > 800 m) of the basin are generally larger than those over the shallower parts. For example, note the spatial correlation of the darkest shaded area in Fig. 10(a) (mean spectral ratios >2.0) with the deepest (NE) bowl in Fig. 10(j). In contrast, the 0.7–1.2 Hz vertical-component mean spectral ratios generally tend to be large everywhere except in areas with the thinnest sediment cover (thickness < 350 m); an exception is found in the NE bowl, where the mean spectral ratios are between 1.3 and 2.0. This overall pattern of vertical-component mean spectral amplification is further illustrated in Fig. 10(c), which shows the mean spectral ratios on the vertical component along profile AB. Note that the impedance effect, with $T_{\mathrm{SED/BED}} = 1.46$ as discussed in the previous section, only partially explains the maximum spectral ratio of 2.7 in Fig. 10(c). Undoubtedly, the reverberations and surface waves seen in Fig. 3 are major contributors to this spectral ratio.

The E–W- and N–S-component mean spectral ratios (Figs 10d–i) show amplification patterns somewhat different from those for the vertical component. The horizontal-component mean spectral ratios tend to be largest over the steepest dipping, but not the deepest, parts of the basin. For example, the largest E–W-component mean spectral ratios are found at the western boundary of the NW bowl and at the western and eastern boundaries of the NE bowl. The horizontal-component mean spectral ratios from 0.7–1.2 Hz are generally larger than those from 0.2–0.7 Hz by up to a factor of 3.

The observation that the sites of the maximum mean vertical-component ratios at low frequencies overlie the deepest parts of the basin is consistent with the physics of 1-D resonance due to 'vertical interference' (see Bard & Bouchon 1985). In other words, vertically propagating waves with lower frequencies tend to be tuned to thicker layers. To show how this concept applies to the Salt Lake Valley, Fig. 10(k) plots the fundamental *P*-wave (f_0^p) and *S*-wave (f_0^s) resonance frequencies for a layer with a free-surface boundary condition at the top and a rigid boundary at the bottom, i.e.

$$f_0^p = \frac{V_p}{4L}, \tag{14}$$

and

$$f_0^s = \frac{V_s}{4L}, \tag{15}$$

where L is the thickness of the 3-D two-layer basin model layer at selected points along profile AB, and V_p and V_s are the *P*-wave and *S*-wave sediment velocities, respectively (e.g. Rial *et al.* 1992). The values of f_0^p and f_0^s along profile AB are for the most part larger than 0.7 Hz for the western part of the basin with intermediate thickness, but are less

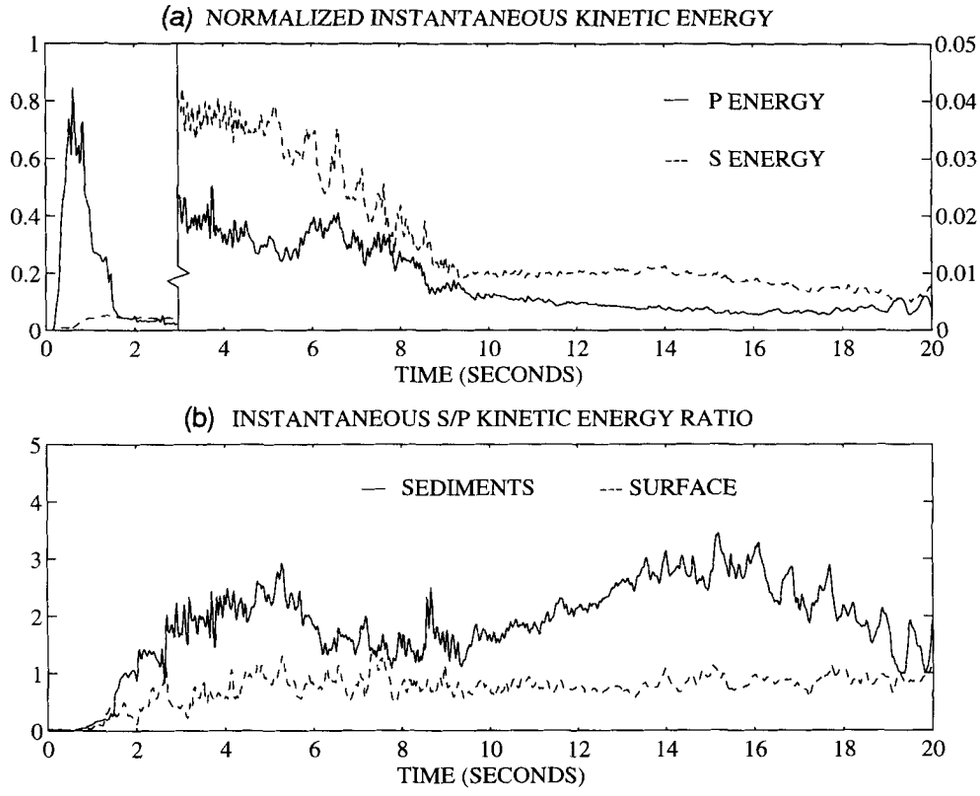

Figure 8. Temporal evolution of the instantaneous P and S energies in a cross-section of the Salt Lake Basin. (a) Average P (solid) and S (dashed) instantaneous kinetic energies in the sediments, and (b) the average S-to-P instantaneous kinetic energy ratios for the sediments (solid) and along the free surface (dashed). All quantities were computed from the vertically incident P-wave response of the 2-D Salt Lake Basin model taken along profile AB in Fig. 3. The kinetic energies in (a) are shown at two different scales where the left (right) axis corresponds to the values before (after) 3 s of simulation.

than 0.7 Hz for the deep north-eastern bowl. Therefore, resonance from vertical interference between 0.2 and 1.2 Hz should be found in the deep, but not in the shallow, parts of the basin. Indeed, this prediction is consistent with the vertical-component mean spectral ratios shown in Figs 10(a)–(c).

Note that the fundamental resonance frequencies for horizontal interference in the Salt Lake Basin along profile AB are much less than those for vertical interference because the basin is much wider than it is deep. The fundamental resonance frequency for horizontal interference of waves in a rectangular inclusion with rigid boundaries at the sides is given by

$$f_0 = \frac{V}{2W}, \tag{16}$$

where W is the width of the inclusion. For example, the NE bowl of the basin is 1.3 km deep compared with its approximate diameter of 10 km; this means that the fundamental resonance frequency for vertical interference is about four times that for horizontal interference. Since the laterally propagating waves are mostly S waves or surface waves for the simulation with a vertically incident plane P wave (see Fig. 3), the fundamental resonance frequency for horizontal interference is much less than the lowest source frequency of 0.2 Hz.

Our analysis of the mean spectral ratio maps in Fig. 10 suggests that resonance in the two-layer Salt Lake Basin model is characterized by vertical interference. This is consistent with Bard & Bouchon's (1985, p. 536) claim that 'the fundamental resonance frequency of all valleys may be satisfactorily estimated using simple formula...' For two-layer 2-D basins with a sinusoidal shape, their formula for the P-wave resonance frequency is

$$f_0^P\sqrt{1+r^2}, \tag{17}$$

and for the SV-wave resonance frequency is

$$f_0^S\sqrt{1+(2.9r)^2}, \tag{18}$$

where $r = h/l$ is the valley's shape ratio, i.e. the ratio of the valley depth h to its half-width l. For the three bowls in the Salt Lake Basin model (Fig. 1a), the NE bowl has a maximum shape ratio of

$$r \approx \frac{1.3\text{ km}}{5\text{ km}} = 0.26, \tag{19}$$

and the NW and southern bowls both have shape ratios less than one-half of this value. The fundamental P-wave and SV-wave resonance frequencies computed from eqs (16) and (17) for the NE bowl of the Salt Lake Basin differ by only 3 and 25 per cent from the 1-D values given by f_0^P and f_0^S, respectively.

Bard & Bouchon (1985) also characterized the type of

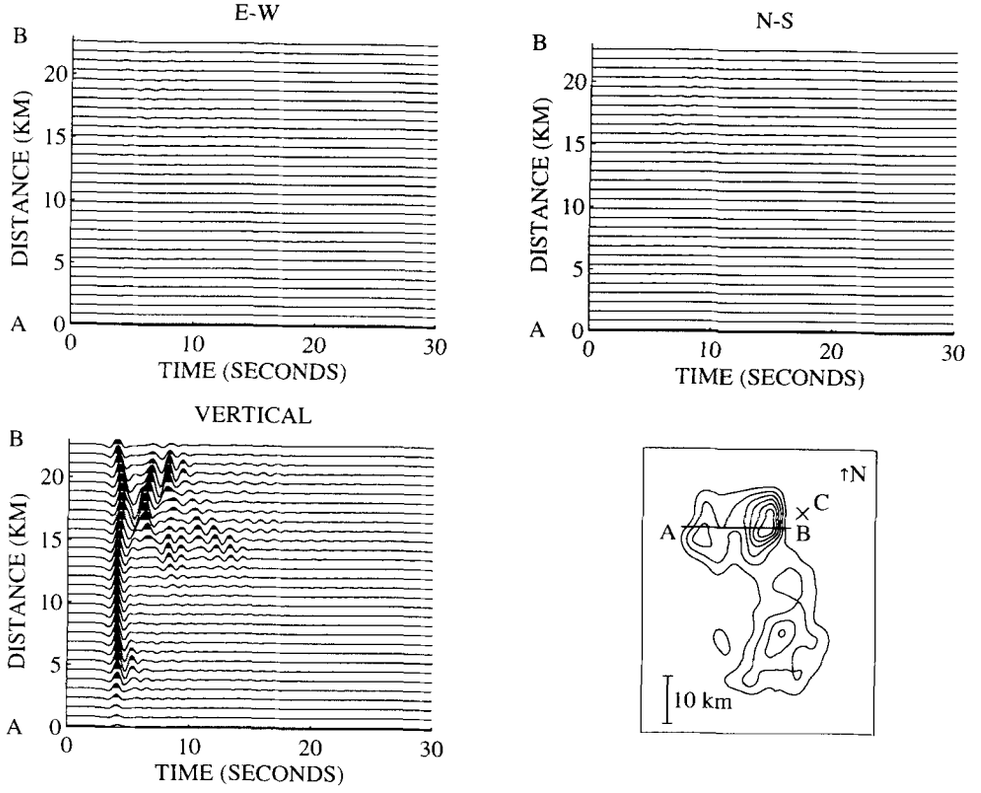

Figure 9. E–W-, N–S-, and vertical-component velocity seismograms for an acoustic simulation with a vertically incident plane *P* wave in the two-layer 3-D basin model. The seismograms are for sites along profile AB shown on the map. The seismic amplitudes are directly comparable to those shown in Figs 3, 12 and 13. The contour map shows the depth to the R2 interface at a contour interval of 200 m. The shallowest contour is at a depth of 150 m below the valley floor. 'x' indicates the location of the reference rock site C.

wave propagation in a sine-shaped valley by defining a critical shape ratio $r_{crit}(C_v)$ as a function of sediment–bedrock velocity contrast C_v. For incident plane *SH* waves, they find that basins with $r > r^{SH}_{crit}(C_v)$ are characterized by 2-D resonance, whereas basins with $r < r^{SH}_{crit}(C_v)$ are characterized by 1-D resonance + lateral wave propagation. For example, Fig. 11 plots $r^{SH}_{crit}(C_v)$ for plane *SH* waves vertically incident onto sine-shaped valleys with $0 < C_v < 8$.

Table 3. Ratios of maximum 3-D acoustic to maximum 3-D elastic ground motion parameters along profile AB (Fig. 3) for simulations with vertically incident *P* waves.

Component	Ground motion parameter	Acoustic/elastic ratio
E-W	Peak particle velocity	0.08
N-S	Peak particle velocity	0.11
Vertical	Peak particle velocity	1.33
E-W	Cumulative kinetic energy	0.007
N-S	Cumulative kinetic energy	0.01
Vertical	Cumulative kinetic energy	1.54
E-W	Signal duration	0.06
N-S	Signal duration	0.04
Vertical	Signal duration	0.55
E-W	Spectral magnitude	0.13
N-S	Spectral magnitude	0.08
Vertical	Spectral magnitude	1.23

The plane wave is assumed to be monochromatic with a frequency nearly equal to that of the basin's 1-D fundamental frequency for *SH* waves. The asterisk in Fig. 11 represents the shape ratio of the NE bowl plotted against the Salt Lake Basin's velocity contrast ratio, which is the same for both *S* and *P* waves:

$$C_v = \frac{2.89\ \text{km s}^{-1}}{1.27\ \text{km s}^{-1}} = \frac{5.0\ \text{km s}^{-1}}{2.2\ \text{km s}^{-1}} = 2.3. \quad (20)$$

The shape ratio of the NE bowl clearly falls below the $r^{SH}_{crit}(C_v)$ curve, suggesting that *SH*-wave propagation in the NE bowl of Salt Lake Basin is characterized by 1-D resonance + lateral wave propagation. This conclusion assumes that the lateral propagation of waves (i.e. Love waves) is primarily along one azimuth, so that the 3-D bowl seismically 'acts' as a 2-D sine-shaped valley. The synthetic seismograms in Fig. 3 lend some support to this assumption.

What about the critical shape ratios for incident plane *P* waves? Does the shape ratio for the NE bowl fall above or below the corresponding critical shape ratio curve? Unfortunately, the $r^{P}_{crit}(C_v)$ curve was not computed by Bard & Bouchon (1985) but they argued that $r^{P}_{crit}(C_v) > r^{SH}_{crit}(C_v)$. Hence the seismic response of the NE bowl to a vertically incident plane *P* wave should also be characterized by 1-D resonance + lateral wave propagation—subject to assumptions analogous to those mentioned above for the case of the incident *SH* wave.

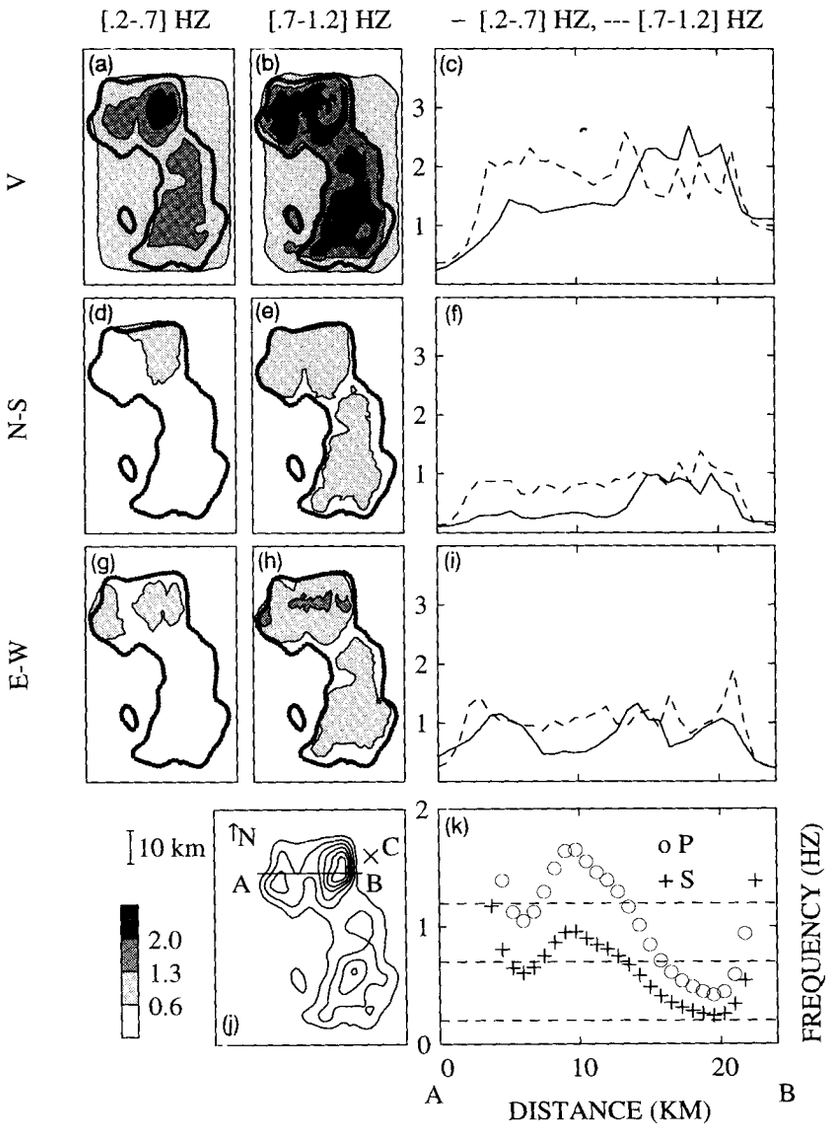

Figure 10. Vertical- (a–c), E–W- (d–f) and N–S-component (g–i) mean spectral ratios in the bandwidths 0.2 to 0.7 Hz and 0.7 to 1.2 Hz for a simulation with a vertically incident plane *P* wave in the two-layer 3-D Salt Lake Basin model; the mean spectral ratios are shown for the Salt Lake Basin (a–b, d–e and g–h) and along the profile AB (c, f and i) shown on map (j). Closed contour lines with a total line length of less than approximately 16 km are considered beyond the resolution of the modelling and have been discarded from the maps. The spectral ratios shown are the mean spectral magnitude divided by that on the vertical component at the rock site, C, depicted on the contour map (j). The maximum values for both bandwidths of the vertical-, E–W-, and N–S-component mean spectral ratios for the Salt Lake Valley are 3.1, 1.9 and 1.5, respectively. The contours in (j) show the depth to the R2 interface at an interval of 200 m, where the shallowest contour is at a depth of 150 m. (k) Fundamental vertical *P*-wave (circles) and *S*-wave (crosses) resonance frequencies along profile AB. The frequencies 0.2, 0.7 and 1.2 Hz are shown as dashed lines.

2-D AND 3-D AMPLIFICATION EFFECTS

Owing to computer limitations, many seismic hazard studies have been confined to either 1-D (e.g. Wong & Silva 1993; Adan & Rollins 1993) or 2-D modelling (e.g. Benz & Smith 1988; Hill *et al.* 1990) and so did not take account of out-of-the-plane propagation and 3-D mode conversion effects. Recent studies that simulate 3-D wave propagation suggest significant differences among 1-D, 2-D and 3-D basin model responses (e.g. Horike 1988; Horike *et al.* 1990; Frankel 1993). In this section, we examine these differences by computing the seismic plane-wave responses of 1-D, 2-D and 3-D Salt Lake Basin models. This comparison is important, since the outcome of such analyses may alter conclusions based on previous 1-D and 2-D ground motion amplification studies for the Salt Lake Basin, and could show whether 3-D modelling is required to estimate ground motion amplification in the Salt Lake Basin accurately.

Figure 12 shows E–W- and vertical-component velocity seismograms for a 2-D simulation with a vertically incident plane *P* wave. The 2-D model is a vertical cross-section of the two-layer 3-D Salt Lake Basin model taken along profile

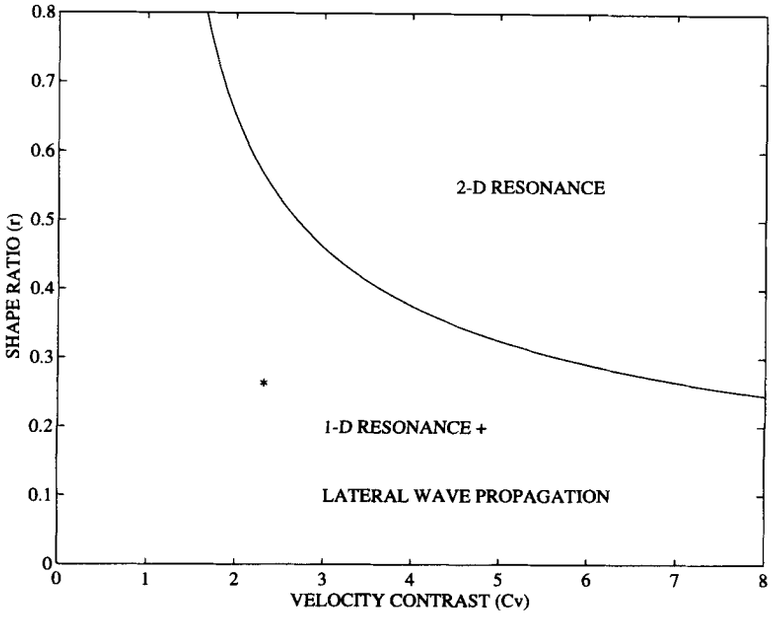

Figure 11. 2-D resonance versus 1-D resonance and lateral wave propagation for *SH* waves vertically incident onto a sine-shaped basin with a shape ratio $r = h/l$ and a velocity contrast C_v. The curve depicts the critical shape ratios $r^{SH}_{crit}(C_v)$ as a function of velocity contrast; a basin (C_v^0, r^0) is characterized by 2-D resonance if its value is plotted above the curve, and is characterized by 1-D resonance + lateral wave propagation if it is plotted below the curve. The value of r for the NE bowl of the two-layer Salt Lake Basin model ($C_v = 2.3$) is plotted as an asterisk (after Bard & Bouchon 1985).

AB. Note the strong similarity between the 2-D (Fig. 12) and 3-D (Fig. 3) responses, especially for the direct *P* waves and the Rayleigh waves generated at the eastern edge of the basin. The main differences are that the 3-D records have longer signal durations. In particular, some durations on the E–W component of the 3-D synthetics are more than a

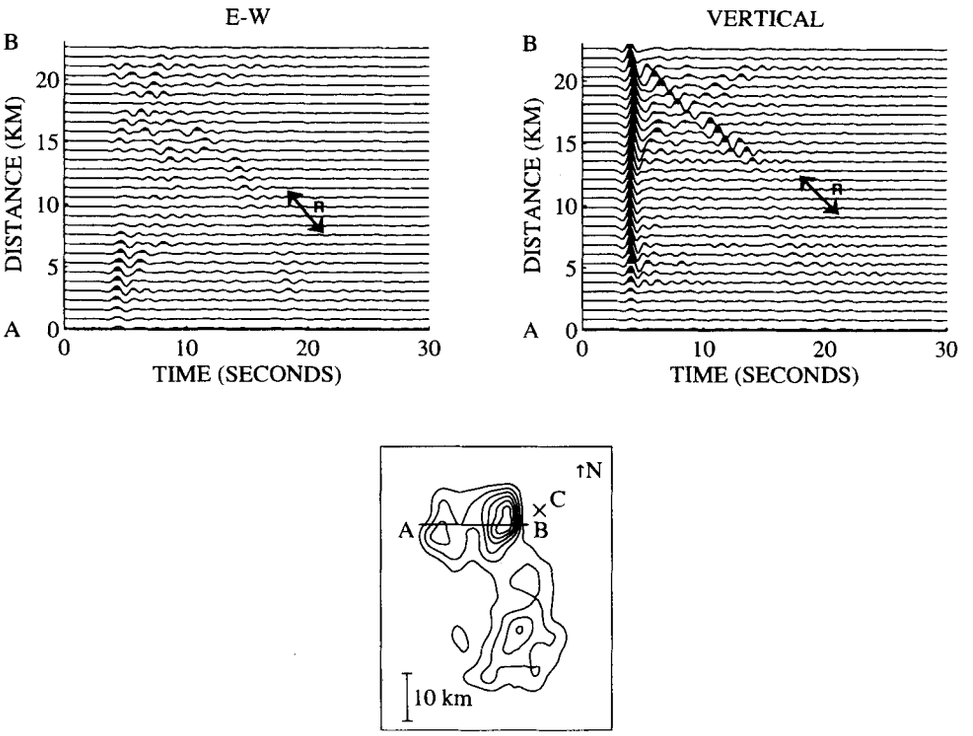

Figure 12. Synthetic E–W- and vertical-component velocity seismograms for a 2-D simulation with a vertically incident plane *P* wave, where the 2-D model is the vertical cross-section of the two-layer Salt Lake Basin model taken along profile AB on the map. 'R' denotes a westward propagating Rayleigh wave generated at the eastern edge of the basin. Amplitudes are directly comparable with those shown in Figs 3, 9 and 13. The contour map shows the depth to the R2 interface at a contour interval of 200 m with the shallowest contour at a depth of 150 m below the valley floor; 'x' indicates the location of the reference rock site C.

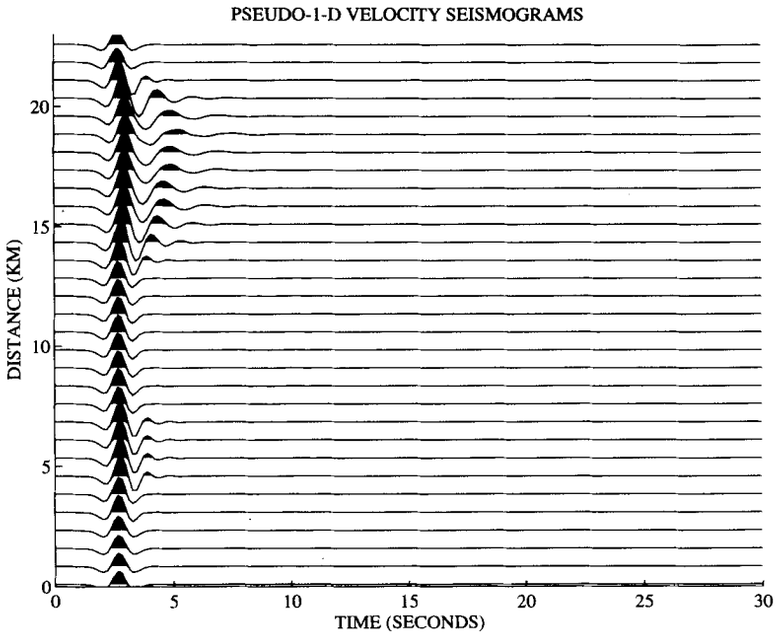

Figure 13. Pseudo-1-D velocity seismograms simulated along profile AB. The pseudo-1-D model response is calculated from plane *P* waves vertically incident on 1-D layer models, where each 1-D model represents the vertical velocity profile directly below a site of interest in the two-layer 3-D Salt Lake Basin model. Amplitudes are directly comparable to those shown in Figs 3, 9 and 12.

factor of 2 longer than those on the E–W component of the 2-D synthetics.

Figure 13 shows pseudo-1-D velocity seismograms along profile AB calculated from 1-D layered representations of the two-layer 3-D Salt Lake Basin model. Note that the signal durations for the 1-D records are much shorter than those for the 2-D (Fig. 12) and 3-D (Fig. 3) records, because of the lack of mode conversion and surface-wave generation in the 1-D layer models.

Figure 14 shows 1-D, 2-D and 3-D ratios of peak particle

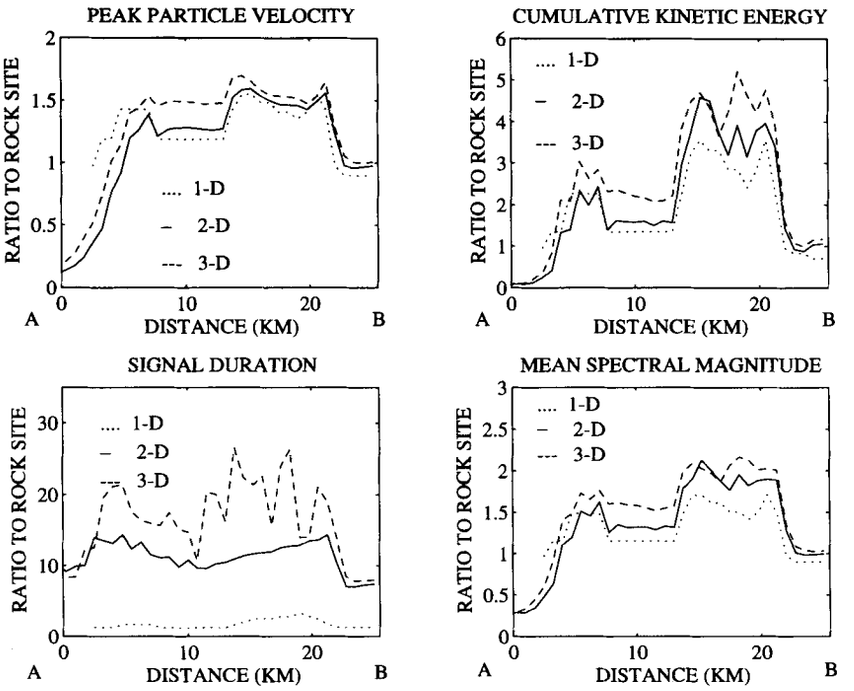

Figure 14. Ratios of vertical-component peak particle velocities, cumulative kinetic energies, signal durations and mean spectral magnitudes along profile AB for 1-D (dotted), 2-D (solid) and 3-D (dashed) simulations with a vertically incident plane *P* wave in the two-layer Salt Lake Basin model. Ratios are computed by dividing the parameter at a valley site by that for the vertical component at the reference rock site C shown in Fig. 12; here, the reference values are taken from the 3-D simulation.

velocities, cumulative kinetic energies, signal durations and mean spectral magnitudes along profile AB. We now compare the 1-D, 2-D and 3-D vertical-component ratios between 7.5 and 21 km along profile AB; this interval is selected to exclude the effects of tapering the plane-wave source at the edges of the 2-D and 3-D models. The 2-D (1-D) ratios underestimate the 3-D values by up to 17 per cent (20 per cent) for peak particle velocities, 40 per cent (48 per cent) for cumulative kinetic energies, 59 per cent (94 per cent) for signal durations, and 22 per cent (34 per cent) for mean spectral magnitudes. The relatively small differences among the 1-D, 2-D and 3-D values for the peak particle velocities agree with the analysis in this paper, which showed that the transmission coefficient of the sediment–bedrock interface accurately predicted the peak particle velocity of the 3-D synthetics. The 2-D, and especially the 1-D, ratios of cumulative kinetic energies, signal durations and mean spectral magnitudes underestimate the 3-D ratios by larger amounts. The 1-D signal durations are much smaller than the 3-D values, which is explained by the absence of 2-D and 3-D scattering, mode conversion, and especially surface-wave generation in the 1-D-layer models.

Figure 15 shows 2-D and 3-D ratios of E–W-component ground motion parameters along profile AB. Again, the ratios are compared between 7.5 and 21 km along profile AB. The 2-D E–W-component ratios underestimate the 3-D values by up to 59 per cent for peak particle velocities, 81 per cent for cumulative kinetic energies, 81 per cent for signal durations, and 51 per cent for mean spectral magnitudes. Except for signal duration ratios, the 3-D ground motion parameter ratios at most sites are predicted by the corresponding 2-D ratios to within a factor of 2. This observation shows that out-of-the-plane focusing, scattering, mode conversion and surface-wave generation account for less than one-half of the E–W component ground motion parameter values along profile AB.

Our results from comparing 1-D, 2-D and 3-D ground motion parameters along profile AB suggest that the 1-D and 2-D values generally underpredict the 3-D values. However, the 3-D vertical-component ground motion parameter ratios roughly match the 2-D (1-D) values to within a scaling factor of 1.1 (1.15) for peak particle velocities, 1.25 (1.7) for cumulative kinetic energies, and 1.1 (1.35) for mean spectral magnitudes. The 2-D ratios of E–W-component peak particle velocities, cumulative kinetic energies, and mean spectral magnitudes must be scaled by factors of 1–2 to approximate the 3-D values.

LIMITATIONS

The primary goal of this paper was to identify the important mechanisms contributing to low-frequency seismic wave amplification in the Salt Lake Basin for simulations with a simple model and source. In this section, we discuss some of the limitations of this study which result from the fact that the simulations we analysed were relatively simple ones.

We have omitted some features from our model which may significantly affect site amplification in the Salt Lake Basin. These features include the following.

(1) Near-surface unconsolidated sediments. Olsen *et al.* (1995a,b) demonstrated the important effects of a near-surface (<300 m) layer of low-velocity (V_p = 1.65 km s^{-1}, V_s = 0.41 km s^{-1}) unconsolidated sediments on

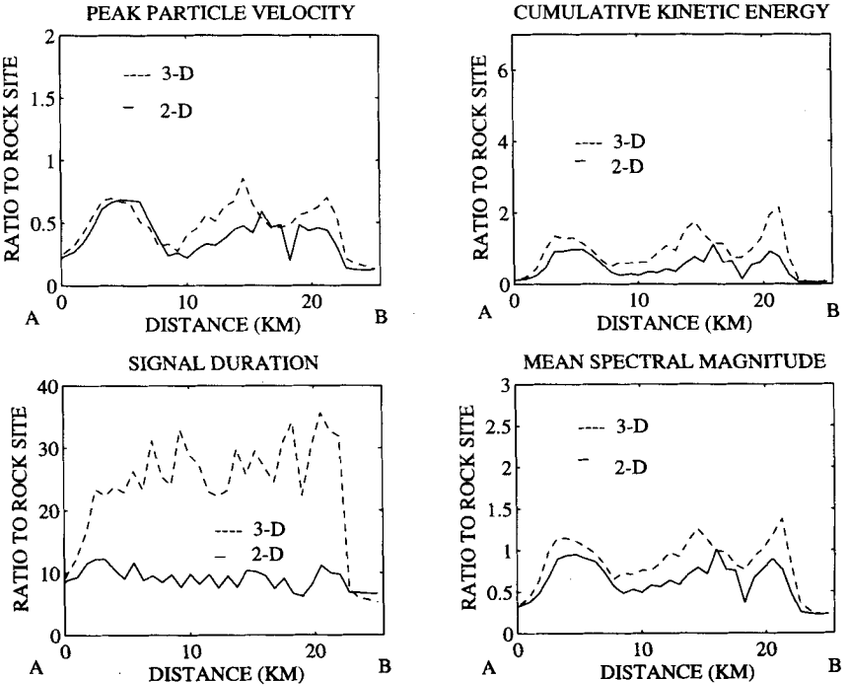

Figure 15. Ratios of E–W-component peak particle velocities, cumulative kinetic energies, signal durations and mean spectral magnitudes in the two-layer Salt Lake Basin model along profile AB shown in Fig. 12; the ratios are computed for vertically incident plane *P* waves in the 3-D (dashed) basin model and in the 2-D cross-section (solid) along profile AB. The reference values are taken as the vertical-component parameters at the rock site C (Fig. 12) for the simulation with a vertically incident plane *P* wave in the 3-D two-layer model.

low-frequency site amplification in the Salt Lake Basin. For simulations of a vertically incident P wave and an open-pit mine blast in a 2-D basin model, they found that including these sediments greatly increased the coda amplitudes and signal durations at some locations in the basin.

(2) Sediment attenuation. From modelling of observed cumulative kinetic energy curves and soil/rock spectral ratios using a 2-D model of the Salt Lake Basin (which included the near-surface unconsolidated sediment layer described above), Olsen *et al.* (1995a,b) found quality factors for the sediments of between 20 and 65. These low Q values have an important influence on ground motions in the Salt Lake Basin.

(3) Topography. This is probably the least important of the three main features omitted in this study. For example, topographic scattering was found to increase the cumulative kinetic energy at a soil site in the 2-D Salt Lake Basin model by 40 per cent or less for simulations with vertically incident P (Olsen *et al.* 1995a) and SH waves (Xu 1995, in preparation).

Another limitation of this study is that the results strictly apply only to the case of a vertically incident P wave—the particular source that we investigated. Earthquake sources radiate a significant amount of S waves. In the following, we discuss how the effects of the mechanisms analysed in this paper might differ for the case of a vertically incident S wave striking the Salt Lake Basin model.

(1) Mode conversions. The transmission coefficient for vertically incident waves at a planar interface dipping 30°—the largest dip of the sediment–bedrock interface in the Salt Lake Basin model—differs by only 20 per cent for SV-to-P and P-to-SV converted waves. We therefore expect mode conversions to be as significant for the case of the vertically incident S wave as for the case of the vertically incident P wave that we modelled.

(2) Impedance effects. In this paper we found that the 1-D transmission coefficient at the sediment–bedrock boundary predicted the amplification of a vertically incident P wave along a profile across our basin model. This result is due to the small dips of the sediment–bedrock interface along most of the profile (as well as elsewhere in our basin model; Fig. 1). Because $V_s = V_p/\sqrt{3}$ for both sediments and bedrock, we expect that impedance effects are similar for vertically incident S and P waves.

(3) Resonance. For our basin model, constructive interference of multiply reflected S waves is tuned to sediment thicknesses that are a factor of $\sqrt{3}$ smaller than those for P waves. At the peak source frequency of 0.6 Hz used in this study, fundamental-mode resonance of vertically interfering waves is obtained for sediment thicknesses of 0.5 km for S waves as compared with 0.9 km for P waves. Assuming that the direct arrival is primarily responsible for initiating vertical resonances (as is indicated by the snapshots in Fig. 6), fundamental-mode resonance of vertically interfering waves will be greatest in the NE bowl for vertically incident P waves (as shown in this paper), and in the NW and southern bowls of the basin model (see Fig. 1) for vertically incident S waves.

(4) Focusing. The degree of bending of vertically incident S waves at the sediment–bedrock interface in the basin model is equal to that for vertically incident P waves, since $V_s = V_p/\sqrt{3}$ for both sediments and bedrock in our basin model.

CONCLUSIONS

We investigated the significance of P-to-S wave conversion, surface-wave generation, impedance effects at the sediment–bedrock interface, resonance, and 2-D and 3-D focusing and scattering for seismic amplification at low frequencies (0.2–1.2 Hz) in a simple two-layer Salt Lake Basin model. For normally incident plane P waves, the results showed the following.

(1) Approximately 30 per cent of the total cumulative kinetic energy on the Salt Lake Valley floor consists of shear-wave energy and surface waves generated by mode conversion. The surface waves appear to be generated primarily along the steeply dipping edges of the basin, which is consistent with the 2-D results of Hill *et al.* (1990) and Murphy (1989). The significance of P-to-S wave conversion is further verified by 2-D simulations that show the instantaneous S/P energy ratio to be as large as 3 in the sedimentary layer.

(2) The largest peak particle velocities along profile AB are always those of the direct P wave. We show that these peak particle velocities can be roughly predicted to within 15 per cent by a simple 1-D estimate of the transmission coefficient.

(3) The vertical-component 0.2–0.7 Hz mean spectral ratios tend to be larger over the deeper parts of the basin than over the shallower parts of the basin. In contrast, the vertical 0.7–1.2 Hz mean spectral ratios tend to be larger over areas that have intermediate sediment thicknesses than over areas with maximum thicknesses. This is consistent with the physics of vertical basin resonance, which predicts that the fundamental resonance frequency should decrease with increasing layer thickness. Since the basin is much wider than it is deep, the seismic response of the two-layer Salt Lake Basin model can be characterized by vertical interference of multiply reflected waves and lateral wave propagation for the bandwidth 0.2–1.2 Hz.

(4) 2-D modelling can roughly predict many of the ground motion parameter values computed by 3-D modelling along a profile across the deepest part of the basin. This result suggests that, in some cases, 2-D modelling may provide fairly accurate predictions of the ground motion parameters in the Salt Lake Basin, which agrees with the results of Olsen *et al.* (1995a). 1-D modelling can generate rough approximations to the 3-D ratios of peak particle velocities, cumulative kinetic energies and mean spectral magnitudes, but not of signal durations.

We have shown that P-to-S wave conversion, surface-wave generation, impedance effects at the sediment–bedrock boundary, and resonance all contribute significantly to low-frequency seismic amplification in a two-layer Salt Lake Basin model. Future attempts to estimate ground motion amplification in the Salt Lake Basin should therefore include the amplification effects of all these processes. 2-D models may yield good approximations to the 3-D ground motion amplification above the deepest part of the Salt Lake Basin, and 1-D simulations can provide rough approxima-

tions to the 3-D amplification for some ground motion parameters.

ACKNOWLEDGMENTS

We would like to thank Dr James C. Pechmann for his thorough review and for useful discussions regarding this work. This research was supported by the National Science Foundation under grant numbers EAR-8816437 and EAR-9104866.

REFERENCES

Adan, S.M. & Rollins, K.M., 1993. Damage potential index mapping for Salt Lake Valley, Utah, *Utah Geol. Surv., Misc Pub.* **93–4**.

Aki, K. & Richards, P.G., 1980. *Quantitative Seismology Theory and Methods,* Vol. I, Freeman and Co., New York, NY.

Anderson, J.G., Bodin, P., Brune, J.N., Prince, J., Singh, S.K., Quaas, R. & Onate, M., 1986. Strong ground motion from the Michoacan, Mexico, earthquake, *Science,* **233,** 1043–1049.

Bard, P.-Y. & Bouchon, M., 1980a. The seismic response of sediment-filled valleys, Part 1. The case of incident SH waves, *Bull. seism. Soc. Am.,* **70,** 1263–1286.

Bard, P.-Y. & Bouchon, M., 1980b. The seismic response of sediment-filled valleys, Part 2. The case of incident P-SV waves, *Bull. seism. Soc. Am.,* **70,** 1921–1941.

Bard, P.-Y. & Bouchon, M., 1985. The two-dimensional resonance of sediment-filled valleys, *Bull. seism. Soc. Am.,* **75,** 519–541.

Bard, P.-Y., Campillo, M., Chavez-Garcia, F.J., & Sanches-Sesma, F.J., 1988. The Mexico earthquake of September 19, 1985: a theoretical investigation of large and small-amplification effects in the Mexico City Valley, *Earthquake Spectra* **4,** 609–633.

Benz, H. & Smith, R.B., 1988. Elastic-wave propagation and site amplification in the Salt Lake Valley, Utah, from simulated normal faulting earthquakes, *Bull. seism. Soc. Am.,* **78,** 1851–1874.

Cerjan, C., Kosloff, D., Kosloff, R. & Reshef, M., 1985. A nonreflecting boundary condition for discrete acoustic and elastic wave equations, *Geophysics,* **50,** 705–708.

Dellinger, J. & Etgen, J., 1990. Wave-field separation in two-dimensional anisotropic media, *Geophysics,* **55,** 914–919.

Frankel, A., 1993. Three-dimensional simulations of ground motions in the San Bernardino Valley, California, for hypothetical earthquakes on the San Andreas Fault, *Bull. seism. Soc. Am.,* **83,** 1020–1041.

Frankel, A. & Vidale, J., 1992. A three-dimensional simulation of seismic waves in the Santa Clara Valley, California, from a Loma Prieta aftershock, *Bull. seism. Soc. Am.,* **82,** 2045–2074.

Frankel, A., Hough, S., Friberg, P. & Busby, R., 1991. Observations of Loma Prieta aftershocks from a dense array in Sunnyvale, California, *Bull. seism. Soc. Am.* **81,** 1900–1922.

Hill, N.R. & Levander, A.L., 1984. Resonances of low-velocity layers with lateral variations, *Bull. seism. Soc. Am.,* **74,** 521–537.

Hill, J., Benz, H., Murphy, M. & Schuster, G.T., 1990. Propagation and resonance of SH waves in the Salt Lake Valley, Utah, *Bull. seism. Soc. Am.,* **80,** 23–42.

Horike, M., 1988. Analysis and simulation of seismic ground motions observed by an array in a sedimentary basin, *J. Phys. Earth,* **36,** 135–154.

Horike, M., Uebayashi, H. & Takeuchi, Y., 1990. Seismic response in three-dimensional sedimentary basin due to plane S wave incidence, *J. Phys. Earth,* **38,** 261–284.

Hough, S.E., 1990. Constraining sediment thickness in the San Francisco Bay area using observed resonances and P-to-S conversions, *Geophys. Res. Lett.,* **9,** 1469–1472.

Joyner, W.B., Warrick, R.E., & Fumal, T.E., 1981. The effect of Quaternary alluvium on strong ground motion in the Coyote Lake, California earthquake of 1979, *Bull. seism. Soc. Am.,* **71,** 1333–1349.

Kawase, H. & Aki, K., 1989. A study on the response of a soft basin for incident S, P and Rayleigh waves with special reference to the long duration observed in Mexico City, *Bull. seism. Soc. Am.,* **79,** 1361–1382.

Levander, A.R., 1988. Fourth-order finite-difference P–SV seismograms, *Geophysics,* **53,** 1425–1436.

Murphy, M., 1989. Finite-difference simulation of seismic P- and SV-wave amplification in the Salt Lake Valley, Utah, *MSc thesis,* University of Utah, Salt Lake City.

Nicholson, C. & Simpson, D.W., 1985. Changes in V_p/V_s with depth: implications for appropriate velocity models, improved earthquake locations, and material properties of the upper crust, *Bull. seism. Soc. Am.,* **75,** 1105–1123.

Olsen, K.B., 1994. Simulation of three-dimensional wave propagation in the Salt Lake Basin, *PhD thesis,* University of Utah, Salt Lake City.

Olsen, K.B., Pechmann J.C. & Schuster, G.T., 1995a. Simulation of 3-D elastic wave propagation in the Salt Lake Basin, *Bull. seism. Soc. Am.* (in press).

Olsen, K.B., Pechmann, J.C. & Schuster, G.T., 1995b. An analysis of simulated and observed blast records in the Salt Lake Basin, *Bull. seism. Soc. Am.* (submitted).

Radkins, H., 1990. Bedrock topography of the Salt Lake Valley, Utah, from constrained inversion of gravity data, *MSc thesis,* University of Utah, Salt Lake City.

Rial, J.A., Saltzman, N.G. & Ling, H., 1992. Earthquake-induced resonance in sedimentary basins, *American Scientist,* **80,** 566–578.

Telford, W.M., Geldart, L.P., Sheriff, R.E. & Keys, D.A., 1976. *Applied Geophysics,* Cambridge University Press, Cambridge.

US Geological Survey Staff, 1990. The Loma Prieta, California, earthquake: An anticipated event, *Science,* **247,** 286–293.

Vidale, J.E. & Helmberger, D.V., 1988. Elastic finite-difference modeling of the 1971 San Fernando, California earthquake, *Bull. seism. Soc. Am.,* **78,** 122–141.

Virieux, J., 1986. P–SV wave propagation in heterogeneous media: Velocity-stress finite-difference method, *Geophysics,* **51,** 889–901.

Williams, R.A., King, K.W., & Tinsley, J.C., 1993. Site response estimates in Salt Lake Valley, Utah, from borehole seismic velocities, *Bull. seism. Soc. Am.,* **83,** 862–889.

Wong, I.G. & Silva, W.J., 1993. Site-specific strong ground motion estimates for the Salt Lake Valley, Utah, *Utah Geol. Surv., Misc. Pub.* **93–9**.

Yomogida, K. & Etgen, J.T., 1993. 3-D wave propagation in the Los Angeles Basin for the Whittier-Narrows Earthquake, *Bull. seism. Soc. Am.,* **83,** 1325–1344.